High-resolution Observations of an X6.4 Solar Flare in the Mid-infrared

Xu Yang; Wenda Cao; Meiqi Wang; Don Jennings; Jiong Qiu; Wen He; Solomon M. Perriyil; Vasyl Yurchyshyn; Lyndsay Fletcher; Paulo J. A. Simões; Murzy Jhabvala; Allen Lunsford; Xingyao Chen; Hugh Hudson

The Astrophysical Journal Letters, 988:L56 (10pp), 2025 August 1 https://doi.org/10.3847/2041-8213/adee95

High-resolution Observations of an X6.4 Solar Flare in the Mid-infrared

Xu Yang[1,2], Wenda Cao[1,2], Meiqi Wang[2], Don Jennings[3], Jiong Qiu[4], Wen He[2], Solomon M. Perriyil[5], Vasyl Yurchyshyn[1,2], Lyndsay Fletcher[6,7], Paulo J. A. Simões[5,6], Murzy Jhabvala[3], Allen Lunsford[8], Xingyao Chen[2], and Hugh Hudson[6,9]

[1] Big Bear Solar Observatory, New Jersey Institute of Technology, 40386 N Shore Ln., Big Bear, CA 92314, USA; wenda.cao@njit.edu
[2] Center for Solar-Terrestrial Research, New Jersey Institute of Technology, 323 Martin Luther King Blvd., Newark, NJ 07102-1982, USA
[3] NASA Goddard Space Flight Center, 8800 Greenbelt Rd., Greenbelt, MD, USA
[4] Department of Physics, Montana State University, Bozeman, MT 59717, USA
[5] Center for Radio Astronomy and Astrophysics Mackenzie, School of Engineering, Mackenzie Presbyterian University, São Paulo, Brazil
[6] SUPA School of Physics and Astronomy, University of Glasgow, Glasgow G12 8QQ, UK
[7] Rosseland Centre for Solar Physics, University of Oslo, P.O. Box 1029, Blindern, N-0315, Oslo, Norway
[8] American University, Physics Department, Washington, DC 20016, USA
[9] Space Sciences Laboratory, University of California, Berkeley, CA 94720, USA
Received 2025 April 30; revised 2025 July 7; accepted 2025 July 7; published 2025 July 28

Abstract

We present a unique observation of the X6.4-class flare SOL2024-02-22T22:34 using the Mid-InfraRed Imager (MIRI) at the Goode Solar Telescope. Three ribbon-like flare sources and one unidentified source were detected in MIRI's two mid-infrared (mid-IR) bands at 5.2 and 8.2 μm. The two stronger ribbons displayed maximum mid-IR enhancements of 21% and 18% above quiet-Sun levels and 10% in Helioseismic and Magnetic Imager (HMI) continuum intensity (I_c). The weak ribbon and the unidentified source had maximum mid-IR enhancements of 7% but showed HMI/I_c dimmings, instead of excess emissions. Our result suggests that mid-IR emission forms in a higher layer during the flare and is more sensitive to flare heating than HMI/I_c emission. The MIRI observations have high temporal resolution (2.6 s cadence in these observations) and show apparent source motions. One flare ribbon extends along weak vertical magnetic-field channels in the sunspot umbra, light bridge, and penumbra, with an approximately 30 s delay between HMI/I_c and 8.2 μm emissions. Meanwhile, the unidentified source moved at an apparent speed of 130 km s^{-1} from a mixed-polarity area to one flare ribbon with a strong HMI/I_c enhancement. We studied available hard X-ray/microwave imaging spectroscopy and used nonlinear force-free field extrapolation modeling to identify flare structures. The observational evidence strongly favors the chromospheric origin of the unidentified mid-IR source. Comparison with the X1.0 flare SOL2022-10-02T20:25 indicates that the total amount of high-energy electron (>60 keV) flux density is a key factor in determining the total brightening area and the maximum intensity enhancement in HMI/I_c emissions.

Unified Astronomy Thesaurus concepts: Solar flares (1496); Solar white-light flares (1983); Solar chromosphere (1479); Solar photosphere (1518); Infrared astronomy (786)

Materials only available in the online version of record: animations

1. Introduction

Solar flares and associated coronal mass ejections constitute the most energetic events in the solar system, releasing up to 10^{32} erg of energy over tens of minutes (e.g., L. Fletcher et al. 2011). Their mid-infrared properties (mid-IR; 5 μm < λ < 12 μm) are still relatively unknown, but the continuum in this wavelength range samples the upper photosphere/lower chromosphere in a unique way (K. Ohki & H. S. Hudson 1975).

P. Kaufmann et al. (2013), R. Miteva et al. (2016), and C. G. Giménez de Castro et al. (2018) reported flares, from M2.0 to X9.7, observed using FLIR A20 8–15 μm (30 THz) cameras in São Paulo and Argentina (A. S. Kudaka et al. 2015; F. M. López et al. 2022). In these studies, the 30 THz emission coincides in time with peaks observed at microwave, visible, EUV, and hard X-ray wavelengths. The authors emphasized that the 30 THz (Mid-InfraRed Imager (MIRI) wavelengths) emission exhibited distinct characteristics, showing that the mid-IR is not simply a proxy for white-light flare emission (e.g., D. Neidig 1989). M. Penn et al. (2016) recorded a C7.0 flare in the 5.2 and 8.2 μm with a two-color Quantum Well Infrared Photodetector (QWIP; J. Bundas et al. 2006) camera at the McMath–Pierce telescope, the same camera used in our observations. The dual-band mid-IR observation was consistent with optically thin free–free bremsstrahlung emission. Recently, this event was analyzed more closely by P. J. A. Simões et al. (2024), and the authors found a relative time delay in the mid-IR emission from the flare's two footpoint regions, taking advantage of MIRI's unique properties. This delay could not be readily explained by the time difference between the arrival of free-streaming energetic electrons, the current standard model for white-light flares. F. M. López et al. (2022) also presented observations of a C2.0 flare at 10 μm and microwave, and considered thermal conduction to be the primary mechanism responsible for the transport of flare energy, given the lack of nonthermal emission signatures in microwaves and hard X-ray (HXR). In the near-IR, Y. Xu et al. (2004) and X. Yang et al. (2025) reported enhancement at the continuum at 1.56 μm during X10

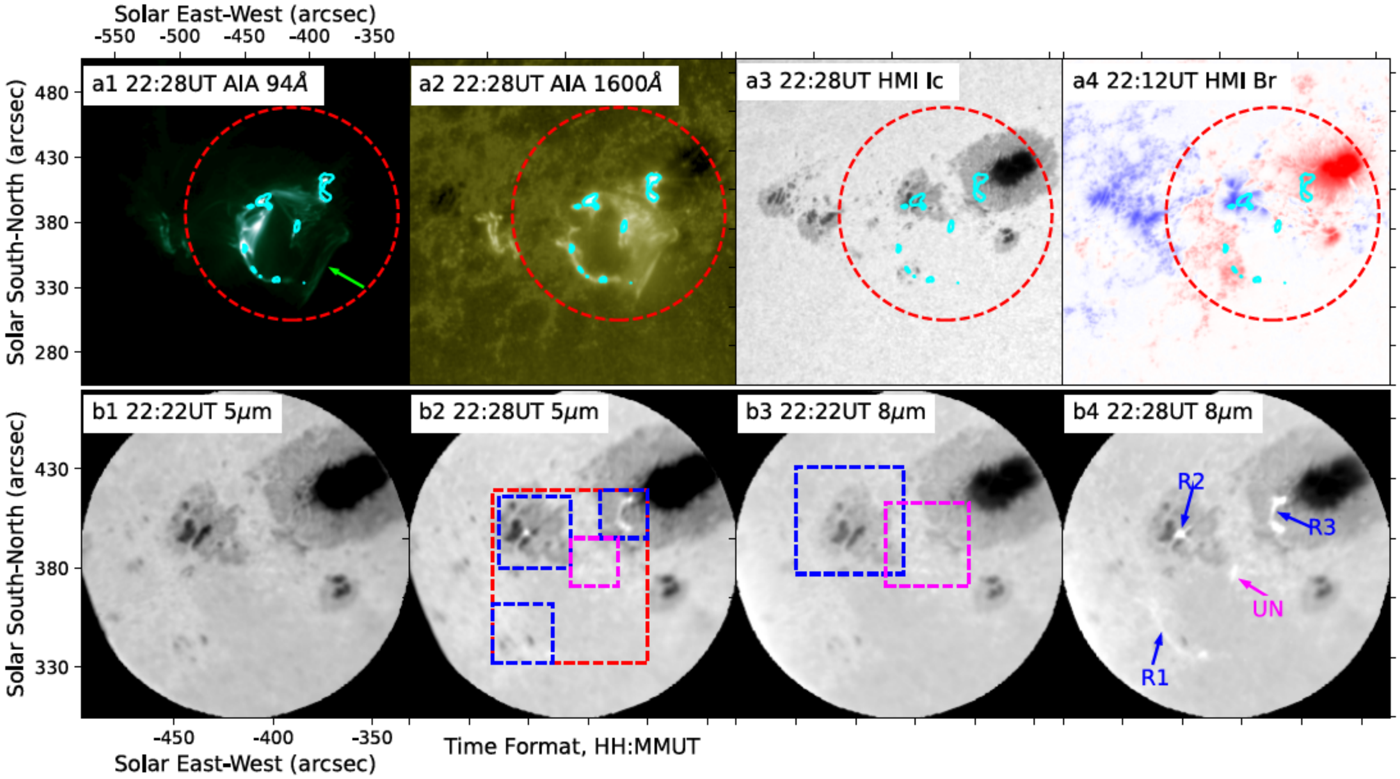

Figure 1. Overview of the X6.4 flare SOL2024-02-22T22:34. Top panels present coaligned AIA 94 Å, AIA 1600 Å, HMI/I_c, and vertical magnetic field B_r imaging data of AR 13590, respectively. The red-dashed circles mark the FOV of MIRI in the lower panels. The green arrow in panel (a1) indicates a jet from an erupted mini-filament. Panels (b1) and (b3) present preflare images in the MIRI 5.2 and 8.2 μm channels, respectively. Panels (b2) and (b4) show the flare brightening in the two IR channels. Cyan contours in panels (a1)–(a4) correspond to 2.7% enhanced intensity (of quiet-Sun area) from the 8.2 μm channel during the flare. Significant brightening is detected in three flare ribbon sources (R1, R2, and R3) and one unidentified source (UN). The rectangles show the areas in panel (b2) selected to calculate the flare light curves; the rectangles in panel (b3) are selected to present the R2 and UN evolution shown in Figures 3 and 4, respectively. An accompanying animation shows the flare evolution in AIA 94 Å, 1600 Å, HMI/I_c, and MIRI 8.2 μm from 22:21 to 22:39 UT.

(An animation of this figure is available in the online article.)

and X1.0 flares, and L. Kleint et al. (2016) analyzed the near-IR continuum near the He I 10830 Å in a X1.0 flare.

G. Trottet et al. (2015) studied the M7.9 flare from P. Kaufmann et al. (2013) across multiple wavelengths, attributing the 30 THz emission to a combination of 80% optically thin chromospheric emission (T 8000 K) and 20% optically thick emission from below the temperature minimum region (T 5000 K). P. J. A. Simões et al. (2017) employed the one-dimensional radiation hydrodynamics code RADYN (M. Carlsson & R. F. Stein 1992), demonstrating that the enhanced mid-IR continuum primarily originates in the chromosphere via the ion free–free mechanism, due to the ionization of H.

In this study, we present observations of SOL2024-02-22T22:34, a GOES X6.4-class flare exhibiting unique mid-IR signatures. Section 2 details the instruments, observations, and data reduction. Section 3 presents a detailed flare data analysis, with Section 3.1 examining the evolution of a flare ribbon in relation to the vertical magnetic field, and Section 3.2 investigating an enigmatic mid-IR source and its potential origins. We restrict our attention here to morphological development, rather than quantitative interpretation of the spectral information, noting, though, that photometric calibration via reference to nonflaring regions is stable and well understood. These observations are among the first mid-IR observations of flares with such good spatial resolution and temporal cadence.

2. Observations and Methods

On 2024 February 22, a GOES X6.4 flare erupted in NOAA Active Region (AR) 13590 (located at −450 , 380 , $\mu = \cos\theta = 0.75$) and was observed using MIRI on the Goode Solar Telescope (GST; P. R. Goode & W. Cao 2012), the Expanded Owens Valley Solar Array (EOVSA; D. E. Gary et al. 2018), the Solar Dynamics Observatory (SDO; P. H. Scherrer et al. 2011), and the Solar Orbiter (SolO; W. B. Atwood et al. 2009). GST monitored the active region from 18:30 to 23:00 UT, with our analysis focusing on the interval between 22:21 and 22:40 UT, with MIRI capturing features including ribbon structures and possibly a loop as well. MIRI employs a two-color QWIP focal plane array, with channels centered at 5.2 μm (4.2–6.2 μm bandwidth) and 8.2 μm (7.0–9.3 μm bandwidth). The detector has a field of view (FOV) of 320 × 256 pixels (0$''$.67 pixel), sufficient to cover a substantial portion of the AR. Level-1 images were cropped to a 165 -diameter circular FOV, with a 2.6 s temporal cadence during flare observations. Data between 22:29:09 and 22:30:01 UT were excluded due to distorted seeing.

EOVSA provided microwave spectroscopy across 1–18 GHz at a 1 s cadence, processed and calibrated using CASA (J. P. McMullin et al. 2007) and integrated to 12 s resolution. SolO/STIX (S. Krucker et al. 2020) contributed X-ray observations in the 4–150 keV range, with images reconstructed via the Maximum Entropy Method (P. Massa et al. 2020). Due to the flare's intensity, STIX operated with its

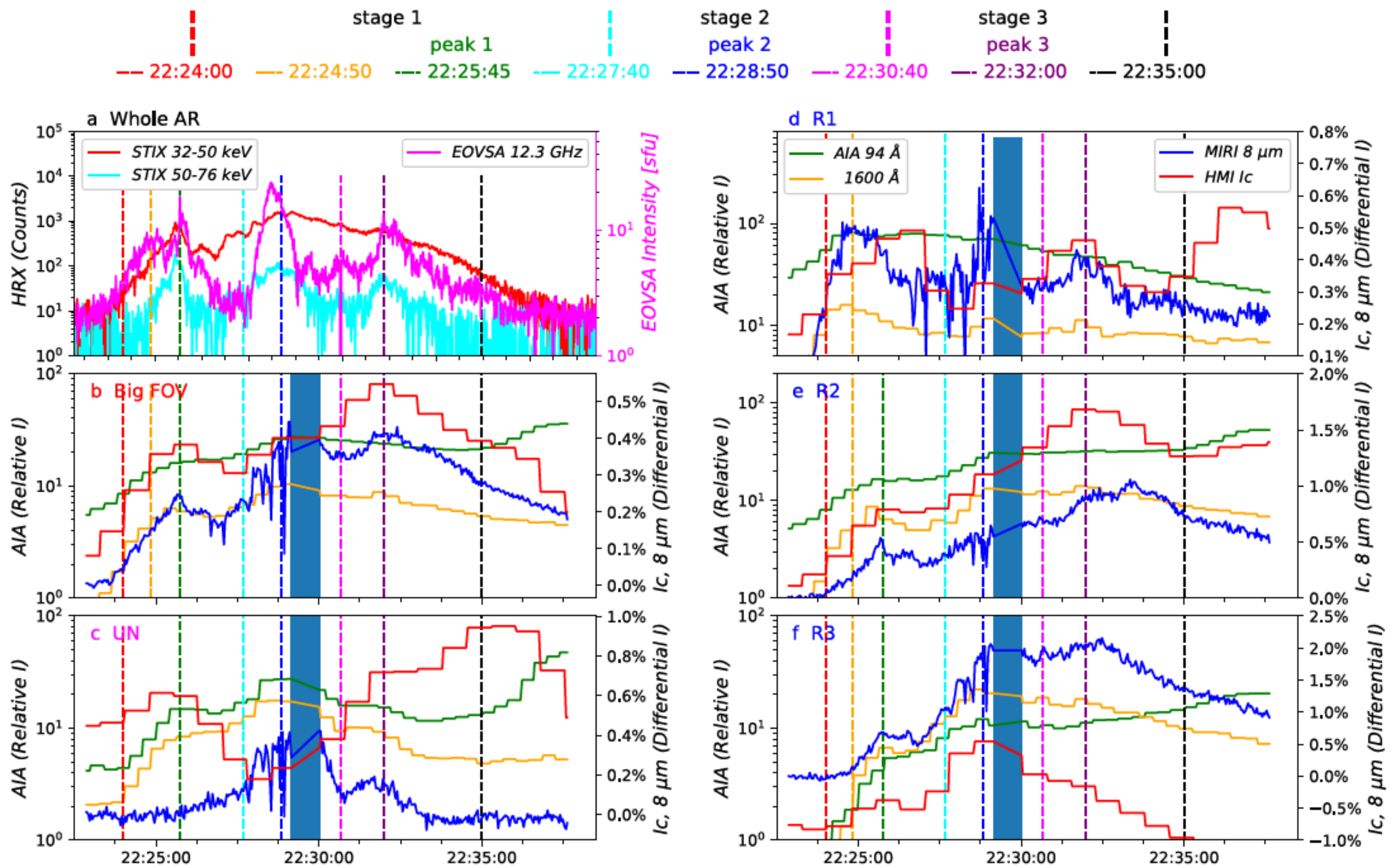

Figure 2. Flare light-curves (LCs) in multiple wavelengths. Panel (a) plots the high-energy HXR (red: 32–50 keV; cyan: 50–76 keV) and high-frequency microwave (magenta: 12.3 GHz) Panels (b)–(f) plot LCs of AIA 94 Å (green), 1600 Å (orange), HMI/I_c (red), and MIRI/8.2 μm (blue) integrated over the selected areas. The baseline intensity for each wavelength is defined as the average during 22:22:00–22:23:00 UT. AIA 94 and 1600 Å LCs are normalized to their base intensity levels. HMI/I_c and MIRI/8.2 μm LCs are presented as percentage deviations from their baseline levels. The shaded regions in panels (b)–(f) mark a weather-impacted period (22:29:06–22:30:01 UT) of relatively low data quality.

attenuator inserted; thus, light curves were derived from the background detector (unaffected by attenuation) and corrected for SolO's heliocentric distance. STIX sources were reprojected and coaligned with SDO/Atmospheric Imaging Assembly (AIA; J. R. Lemen et al. 2011) maps.

SDO/AIA provided UV/EUV imaging; however, most channels were saturated during this X6.4 flare. We analyzed unsaturated AIA 94 Å images taken with a short exposure time and 1600 Å images to study the flare ribbons and loops. Photospheric continuum intensity (I_c) images at a cadence of 45 s, and the vector magnetic field measurements were provided by the Helioseismic and Magnetic Imager (HMI; J. Schou et al. 2011).

All data sets were spatially coaligned to a reference time of 22:28 UT, using a full-disk SDO/HMI I_c image as the fiducial. The image time series in each data set was then aligned to the reference time. Image registration and coalignment follow the algorithm described in X. Yang et al. (2022). We apply a nonlinear force-free-field extrapolation method with a conservation-element and solution-element scheme (CESE-MHD-NLFFF; C. Jiang et al. 2011; C. Jiang & X. Feng 2013) to reconstruct the three-dimensional coronal magnetic field under a force-free assumption. The photospheric vector magnetograms at 22:12 UT from SDO/HMI, Space-weather HMI Active Region Patch (SHARP; M. G. Bobra et al. 2014) data product, are used as the lower boundary condition for the NLFFF method. To approach the force-free assumption, the original photospheric vector magnetograms were preprocessed following the basic approach of T. Wiegelmann et al. (2006). Then, we obtain a converged result from the extrapolation and perform a routine check of the result with a series of NLFFF quality metrics (C. Jiang & X. Feng 2013; W. He et al. 2022).

3. Results

Figure 1 provides an overview of the observation. A circular brightening pattern consisting of flare ribbons and flare loops dominates the AIA images. A mini-filament erupted in the initial phase of the flare (22:22–22:27 UT) and left a coronal jet as indicated by the green arrow in Figure 1(a1). The vertical magnetic field (B_r), derived from HMI vector magnetic field data with azimuthal disambiguation, was obtained 10 minutes prior to flare onset.

GST/MIRI successfully captured infrared flare emissions and resolved four distinct brightening sources within its FOV (Figure 1(b4)). Three of these mid-IR sources exhibited spatial correspondence with flare ribbons (R1, R2, and R3) identified in the AIA 94 and 1600 Å images, while the fourth source remained unidentified (UN). The 8.2 μm emission was enhanced to a maximum value of 21% and 18% (of quiescent value in a quiet area) in R2 and R3 after the flare peak around 22:28:50 UT. The 8.2 μm emissions in R1 and UN increased to a maximum of 7%. At 8.2μm and at the maximum emission, the excess flare brightness temperature T_b was estimated as

980 K for R2, 850 K for R3, and 330 K for R1 and UN. At 5.2 μm, the signal is weaker relative to the background. The contrast is 9% in R2, 6% in R3, 5% in R1, and 4% in UN. The corresponding flare excess T_b is 430, 280, 235, and 190 K, respectively. HMI/I_c emission from R2 and R3 increased by 10% at their peaks, while R1 and UN did not show significant brightening.

Figure 2 provides multiwavelength light curves (LCs) from HXR to mid-IR emission. Based on the HXR and microwave LCs, this flare can be divided into three stages, each marked by a prominent peak.

Stage 1 (22:24:00–22:27:40 UT), characterized by its peak at 22:25:45 UT, represents a preflare phase. In this stage, multiple locations within the AR exhibited enhanced emission, while the unidentified source (UN) remained inactive. The mini-filament mentioned above erupted during this period. In R2 and R3 areas, EUV, UV, and mid-IR LCs agreed with the white-light (WL) LCs, and all of them peaked around 22:25:45 UT. However, the differences are also notable: HXR peaked at 22:25:33 UT, which is 12 s earlier than the microwave, which is not uncommon (A. V. R. Silva et al. 2000). In contrast, the R1 region displayed earlier brightening, with AIA 94 Å, 1600 Å, and MIRI/8.2 μm emission all peaked at 22:24:50 UT (Figure 2(d), orange vertical dashed lines) earlier than the first HXR/microwave peak. These early simultaneous peaks in 94 and 1600 Å could indicate initial heating at the footpoints (P. J. A. Simões et al. 2024). A corresponding minor peak in the microwave LC aligns with this early brightening phase, potentially associated with the flare trigger mechanism.

Stage 2 (22:27:40–22:30:40 UT) represented the main phase of the flare. During this period, the microwave peaked at 22:28:30 UT, which is 20 s earlier than the HXR. HXR, AIA 94 Å, 1600 Å, and MIRI/8.2 μm LCs exhibited nearly simultaneous peaks across all sources around 22:28:50 UT. However, HMI/I_c emissions displayed significantly different behaviors. While R2 and R3 showed coordinated intensity increases with other wavelengths, both R1 and UN exhibited distinct dips in their HMI/I_c LCs. This contrast in HMI/I_c response suggests the presence of two distinct heating mechanisms in different flare substructures.

Stage 3 (22:30:40–22:35:00 UT) manifested as a small peak in both high-frequency microwave and high-energy HXR LCs. Meanwhile, corresponding minor enhancements also appeared in other wavelengths (Figure 2). However, these enhancements mixed with the cooling process in stage 2, making it difficult to analyze the heating mechanism during this stage. Temporal analysis revealed different cooling behaviors between flare ribbons. Despite the 45 s cadence of HMI/I_c, R2 exhibited an approximately 40 s delay (22:32:40–22:33:20 UT) between HMI/I_c and mid-IR peaks during Stage 3. R3 showed essentially no temporal offset (peak at 22:28:50 UT) during Stage 2. This differential cooling pattern suggests varying thermal properties or energy deposition profiles between the two ribbon structures.

We performed HXR spectral analysis within 15 s before and after the peak time of 22:28:50 UT. The STIX attenuator was inserted during the event, affecting the photon flux at X-ray energies below 11 keV (S. Krucker et al. 2020). Therefore, we restricted our analysis to the nonthermal energy range above 20 keV. Using the OSPEX package in SSWIDL (R. Schwartz et al. 2002), we applied a single power-law fit to the HXR spectrum.

The derived photon spectra index γ is 7.79 0.10. Under the thick-target (e.g., J. C. Brown 1971) assumption ($= \gamma + 1$), this corresponds to an electron spectral index $= 8.79$ 0.10, while the thin-target model($= \gamma - 1$) gives $= 6.79$ 0.10. Following the methodology of (Equations (2.10) and (2.12) in G. D. Holman et al. 2011), we calculated the nonthermal electron power above 20 keV to be 3.4×10^{30} erg s^{-1} for the thick-target model and 7.5×10^{29} erg s^{-1} for the thin-target model. The total area for the HMI/I_c kernel in R2 and R3 with at least 5% increased intensity of the quiet Sun is measured as 1.29×10^{17} cm^2. Thus, the energy flux density ($> 20keV$) during the flare peak is 2.64×10^{13} erg cm^{-2} s^{-1} for the thick-target model and 5.83×10^{12} erg cm^{-2} s^{-1} for the thin-target model. Meanwhile, the energy flux density of electrons above 60 keV was 1.44×10^{10} erg cm^{-2} s^{-1} in the thick-target model. The STIX/HXR data revealed extremely "soft" spectra during the flare peak. In the discussion, we compare these findings with a previously observed flare (SOL2022-10-02T20:25 X1.0) that presented a comparable HMI/I_c intensity enhancement and kernel area.

3.1. Flare Ribbon and Vertical Magnetic Field

Figure 3 illustrates the fine-scale evolutions observed in flare ribbon R2. R2 originated in a small sunspot area that consisted of two umbrae. These two umbrae were separated by a light bridge, while their B_r polarities were identical (negative polarity). Some brighter channels, inside the dark penumbral area, corresponded to weaker B_r areas. Panel (a1) presents the shear motion resolved in this area by the optical flow method. These surface flow motions may contribute to the ignition of flare reconnection.

Panels (b1)–(b6) of Figure 3 show HMI/I_c (background) and mid-IR (dashed line contours) differential images of R2 at six selected moments. The white solid line contours in each panel mark the dark structures in the HMI/I_c observations. Cyan and dark cyan solid line contours in the middle and lower panels highlight the structures of stronger B_r inside and outside the umbra, respectively. The black "x" symbols indicate the extended part of the mid-IR kernel (compared with the previous time).

The flare footprints showed complex behavior. The mid-IR flare ribbon R2 initially appeared west of the umbrae. Between 22:24:26 and 22:25:57 UT, it propagated into the light bridge through a weak B_r channel within the west umbra. Meanwhile, brightening was observed in flare ribbon R3 (cyan solid line contours in Figure 4). From 22:25:57 to 22:28:12 UT, the mid-IR flare ribbon extended along the light bridge toward both ends. At approximately 22:28:56 UT, it executed a sharp turn at the northern edge of the light bridge and propagated toward the southwest through a weak B_r channel in the penumbra. During 22:28:56–22:30:26 UT, the mid-IR ribbon exhibited an average velocity of 76 km s^{-1} in the plane of sky. Subsequently, the R2 ribbon continued its progress through a weak-field channel situated between two strong magnetic structures (indicated by white and dark cyan contours in the lower right panel).

A temporal delay was observed between the HMI/I_c enhancement and mid-IR brightening as the flare ribbon expanded. At one selected location (blue star in Figure 4 panel (b3)), this delay was measured as 27 s, while at other positions along R2, delays ranged approximately between 25 and 40 s. As the cadence of HMI/I_c is 45 s, the measured delay may not be very precise.

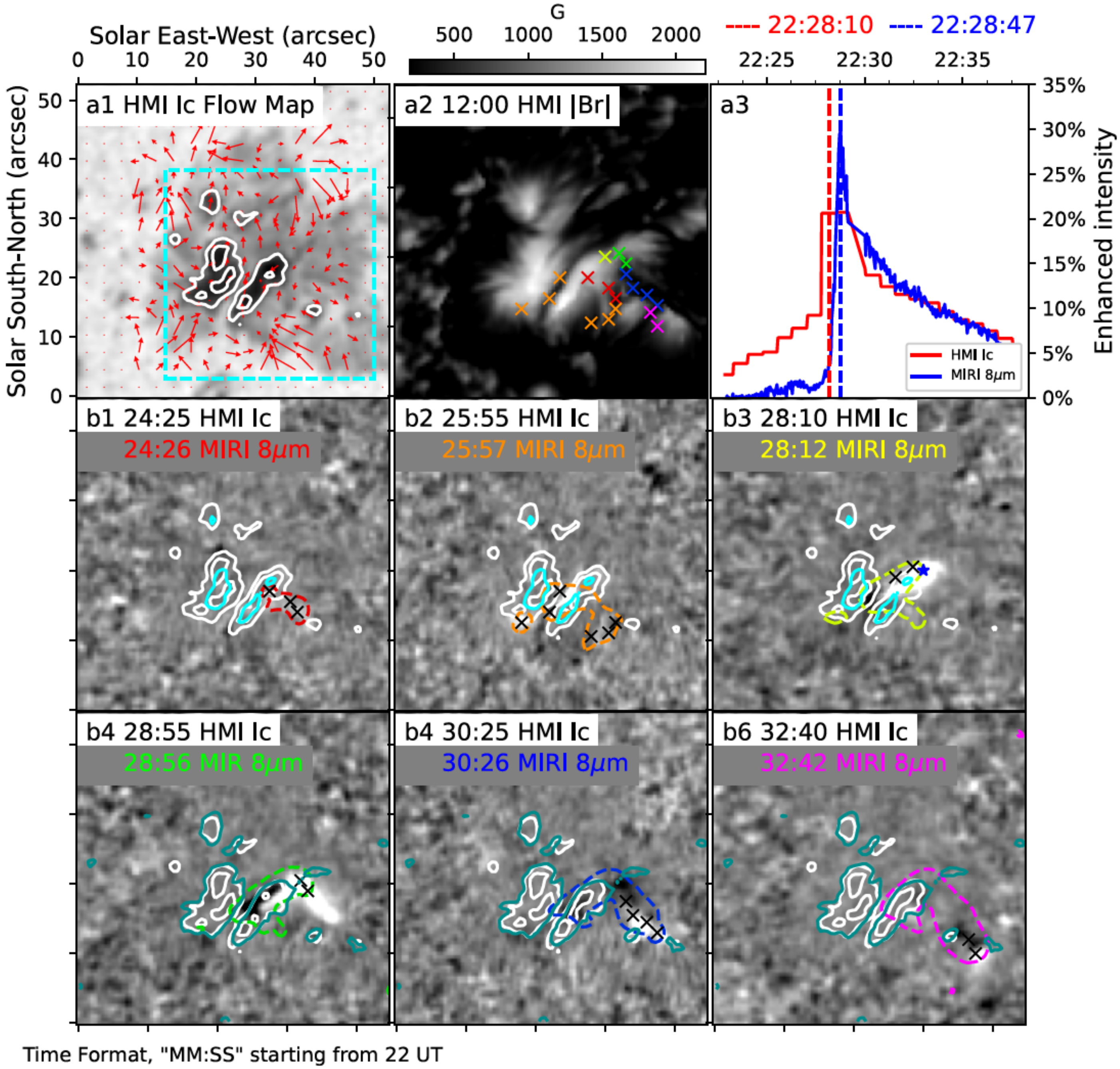

Figure 3. Evolution of the middle flare ribbon (R2). Panel (a1) presents an optical flow map 30 minutes before flare onset. Panel (a2) displays the absolute value of the vertical magnetic field ($|B_r|$). Panel (a3) plots LCs of HMI/I_c (red) and MIRI/8.2 μm (blue) emissions at the "blue star" position marked in panel (b3). The vertical dashed lines indicate the time delay between HMI/I_c peak and MIRI/8.2 μm peak. Panels (b1)–(b6) present the flare ribbon evolution resolved by HMI/I_c running-difference images (grayscale background) and MIRI/8.2 μm base-difference images (dashed line contours). Black crosses ("x") mark locations of extended infrared (IR) brightening at each timestep; these are overplotted in panel (a2) with corresponding colors to trace the IR brightening trajectory. White solid contours outline umbrae and dark pores. Cyan solid line contours in (b1)–(b3) present strong $|B_r|$ (1900 G) structures within the umbrae, while dark cyan solid line contours in (b4)–(b6) mark strong $|B_r|$ (1300 G) structures outside the umbrae. An accompanying animation displays the R2 evolution in AIA 94 Å, 1600 Å, HMI/I_c, and MIRI 8.2 μm from 22:23 to 22:39 UT.

(An animation of this figure is available in the online article.)

3.2. Unidentified Hot Source

As illustrated in Figure 4, a small bright feature (magenta contour) was observed in AIA 94 Å, AIA 1600 Å, and mid-IR channels. This feature propagated from a region of mixed magnetic polarity toward flare ribbon R3 (cyan contour) during 22:27–22:31 UT, which was simultaneous with the flare ribbon R2 turning southwest from the light-bridge north point.

The UN initially appeared as a cluster of bright emission together with complex, spider-web-like coronal loop background structures. As the bright emission approached R3, two fine-scale streams (S1 and S2 in panel (a6)) were resolved within the cluster. S1 and S2 eventually diverged and merged into two different locations in R3. Panel (b) presents the AIA 1600 Å image at the same time as the AIA 94 Å image in panel (a3). While the AIA 1600 Å channel detected a similar bright

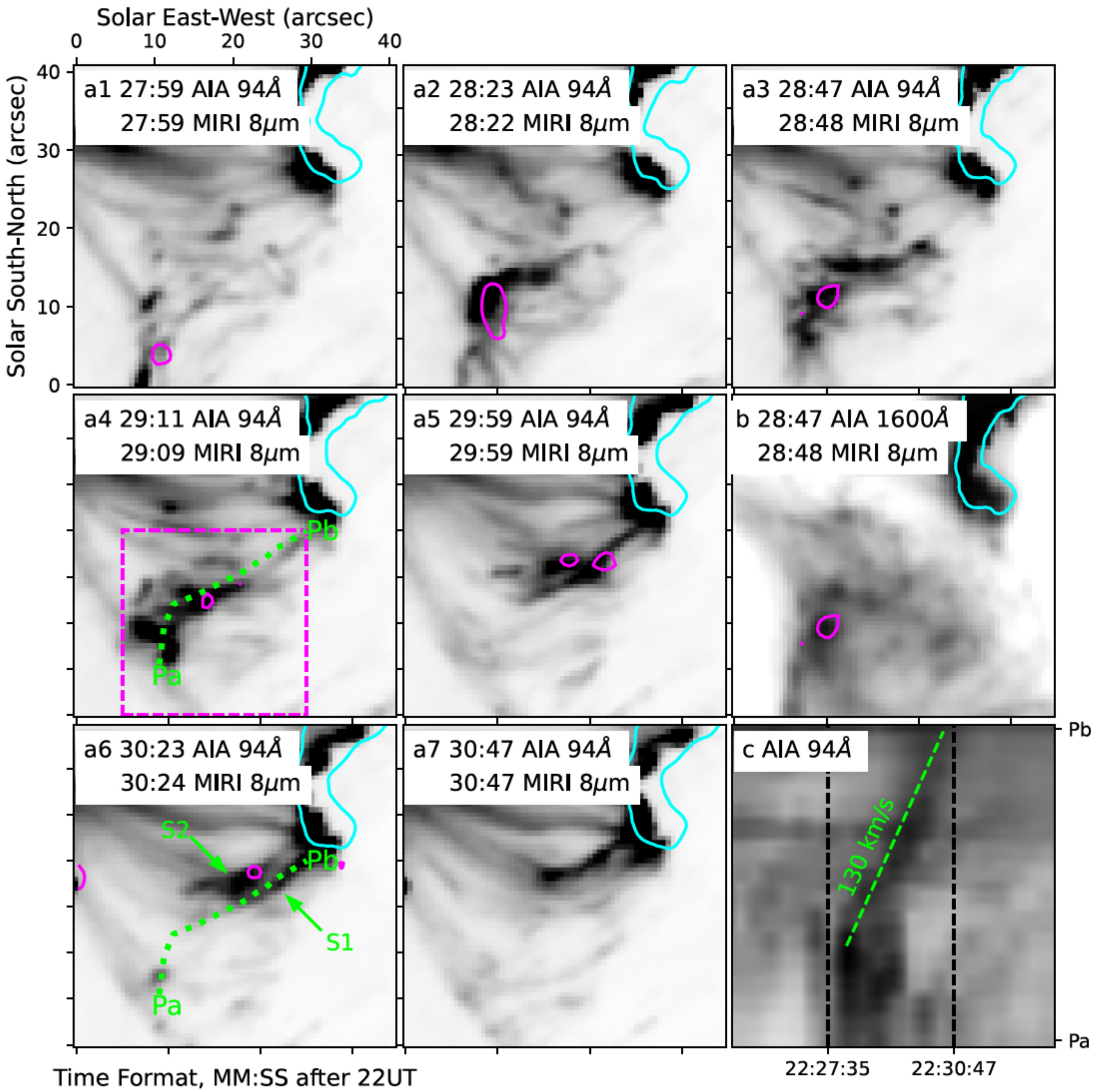

Figure 4. Evolution of the UN. Panels (a1)–(a7) present AIA 94 Å reversed grayscale images showing hot flare loop emission moving toward flare ribbon R3 (cyan contours). Magenta contours mark emission from the UN source (3% enhanced intensity relative to quiet-Sun area) from the MIRI 8.2 μm channel. Two streams (S1 and S2) are resolved in panel (a6). Panel (b) presents AIA 1600 Å image at the same time as in panel (a3). Panel (c) presents a time-distance map along Pa-Pb from AIA 94 Å channel. The black dashed lines in panel (c) indicate 22:27:35 and 22:30:47 UT, respectively.

emission feature, its background presented plage-like structures. Panel (c) presents a time-distance plot extracted from AIA 94 Å data along the trajectory of the UN source (Pa-Pb dashed line in panels (a4) and (a6)). The averaged plane-of-the-sky velocity of the UN source exceeded 130 km s^{-1}.

We illustrate two possibilities to explain the origin of the UN source and test them in Figure 5. Panels (a1) and (a2) display the magnetic field lines derived with the CESE-MHD-NLFFF extrapolation, overlaid on the projected AIA 94 Å and HMI/I_c images. The selected field lines originate from regions with a relatively high squashing factor (Q). The extrapolated field lines correspond well to the coronal loops in the coaligned EUV image.

1. Red field lines connect flare ribbons R1 and R2.
2. Green field lines correspond to the preflare filament, and one end of the footpoints is located in the initial brightening of R2.
3. Magenta and blue field lines are rooted in the two umbrae of R2, constraining the initial brightening

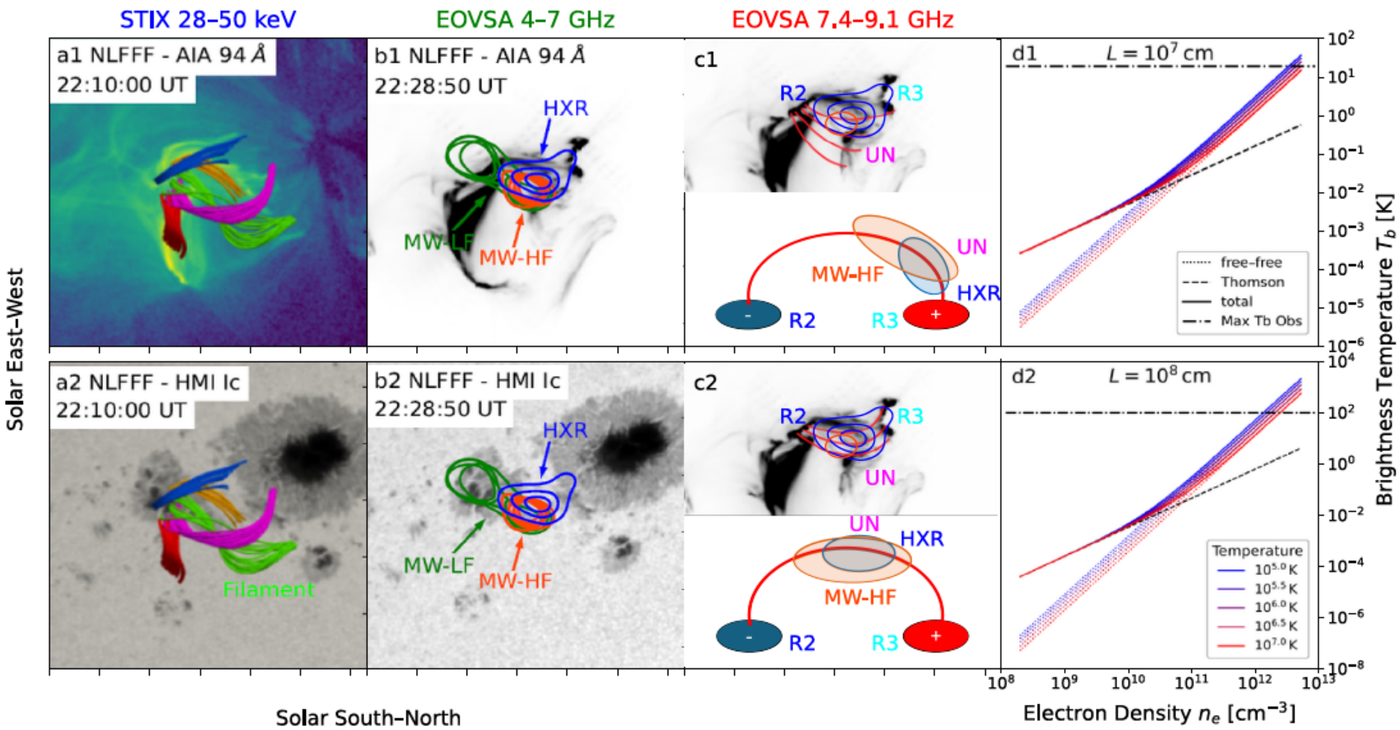

Figure 5. Magnetic field extrapolations and analysis of the UN source. Panels (a1) and (a2) plot magnetic field lines from the CESE-MHD-NLFFF extrapolation over deprojected AIA 94 Å and HMI/I_c images at 22:10 UT. Panels (b1) and (b2) plot STIX/HXR (blue, 28–50 keV) and EOVSA microwave-low-frequency (green, 4–7 GHz) and microwave-high-frequency (orange, 7.4–9.1 GHz) contours over AIA 94 Å and HMI/I_c images at 22:28:12 UT. Panels (c1) and (c2) propose two source distribution speculations for microwave and HXR emissions, with orange solid lines indicating the speculated magnetic loop configurations. Panels (d1) and (d2) modeled brightness temperature T_b at 8.2 μm vs. electron density n_e for two slab depths ($L = 10^7$, 10^8 cm), at temperatures ranging from 10^5 to 10^7 K. The horizontal black dotted line marks the required 336 K brightness temperature excess (7% brightening).

location and aligning with the subsequent flare ribbon extension.

The NLFFF extrapolation supports the hypothesis that the UN source is associated with the flare ribbon. Additionally, orange field lines extend from the northern end of the light bridge to a mixed-polarity region, suggesting a possible secondary reconnection site.

Panels (b1) and (b2) present complementary observations in microwave (EOVSA, 4–9.1 GHz) and hard X-ray (SolO/STIX, 28–50 keV) wavelengths. Then, two plausible explanations for the origin of the UN source are shown: a footpoint configuration in panel (c1) and a looptop configuration in panel (c2).

To evaluate the two proposed scenarios, we conduct a quantitative analysis based on radiative transfer modeling. Consider a uniform plasma layer of thickness L above the solar surface, its specific intensity $I(\nu)$ at frequency ν can be described with the radiative transfer equation

$$I(\nu) = I_0(\nu)\, e^{-\tau(\nu)} + S(\nu)\,(1 - e^{-\tau(\nu)}), \qquad (1)$$

where $I_0(\nu)$ is the background emission, $\tau(\nu) = \kappa(\nu)L$ is the optical depth, and $S(\nu) = j(\nu)/\kappa(\nu)$ is the source function, with $j(\nu)$ and $\kappa(\nu)$ denoting the emission and absorption coefficients. We calculate κ_ν considering ion free–free radiation (P. J. A. Simões et al. 2017) and j_ν considering both ion free–free and Thomson scattering (P. Heinzel et al. 2017; S. Jejcic et al. 2018),

$$I(\nu) = I^{\rm Th}(\nu) + I^{\rm ff}(\nu), \qquad (2)$$

where the free–free opacity (scaling with n_e^2) is highly sensitive to temperature, while Thomson scattering scales linearly with n_e and depends on the diluted photospheric radiation; here we used a dilution factor of 0.354 (P. Heinzel et al. 2017), but we also tested a value of 0.5, without meaningful changes in the results.

Panels (d1) and (d2) in Figure 5 present our quantitative modeling results, exploring variations in electron density ($n_e = 10^8$–10^{13} cm^{-3}), temperature ($T = 10^5$–10^7 K), and layer thickness ($L = 10^7$–10^8 cm). The horizontal black dotted line marks a 330 K (7%) brightness temperature enhancement above the quiet-Sun level, derived from the 8.2 μm observation.

For a thin slab (10^7 cm), the observed 7% brightness enhancement at 8.2 μm requires extremely high electron densities ($n_e \gtrsim 10^{13}$ cm^{-3}), and is more feasibly achieved at lower temperatures. At typical coronal electron densities ($n_e \lesssim 10^{13}$ cm^{-3}), the resulting brightness excess is undetectable with current IR telescopes. As the depth of the slab increases (to 10^8 cm), the threshold electron density to achieve the desired brightness enhancement decreases ($n_e \gtrsim 10^{12.5}$ cm^{-3}). However, even this reduced requirement remains sharply inconsistent with observed coronal loop densities. Note that the Thomson scattering contribution remains negligible for any electron density.

For a typical flaring corona loop situation ($n_e \lesssim 10^{12}$ cm^{-3}), producing detectable mid-IR brightening is highly unlikely. In contrast, a denser ($n_e > 10^{12}$–10^{13} cm^{-3}) slab in the deeper atmosphere readily explains the observations. Therefore, our quantitative analysis suggests that the UN source may have a chromospheric origin, in agreement with prior simulations (P. J. A. Simões et al. 2017).

4. Summary and Discussions

This Letter presents unique high-resolution mid-IR flare observations of SOL2024-02-22T22:34, complemented by multiwavelength data. D. Li et al. (2024) have also studied the quasiperiodic pulsations (QPP) in this event and concluded that the white-light QPP is modulated by slow-mode magnetoacoustic gravity waves leaking from the sunspot penumbra. S. Roy et al. (2025) further analyzed the flare timeseries obtained for the entire flaring region at a 1 minute cadence and concluded that the flare UV emissions are tightly related to HXR, which we can now extend to 1 s cadence. GST/MIRI observed three flare ribbon sources and one unidentified source in the 5.2 and 8.2 μm channels. Taking advantage of high-spatial and high-temporal resolution observation of GST, we conducted a detailed examination of each flare-associated source.

1. The mid-IR emission in this event exhibited a high degree of spatial and temporal correlation with UV and EUV emissions at each mid-IR source. In contrast to a coherent mechanism or due directly to nonthermal excitation, this result strongly suggests a predominantly thermal origin for the observed mid-IR radiation, in agreement with previous works (P. J. A. Simões et al. 2017; F. M. López et al. 2022).
2. Enhanced HMI/I_c emission was detected in the two prominent IR flare ribbon sources (R2 and R3) during flare stage 2. In contrast, transient dips in the HMI/I_c light curves were observed at a weaker IR ribbon source (R1) and the unidentified mid-IR source (UN).
3. High-temporal-resolution IR observations revealed a flare ribbon (R2) propagating along weak magnetic field channels, spanning the sunspot umbra, light bridge, and penumbra. A temporal delay of approximately 30 s was observed between the HMI/I_c emission and the subsequent 8.2 μm emission in this ribbon.
4. The unidentified mid-IR source, UN, exhibited apparent motion at a plane-of-sky velocity of 130 km s^{-1}, migrating from a mixed-polarity region toward a flare ribbon (R3) that displayed a strong HMI/I_c enhancement.

When compared to WL counterparts, the four mid-IR sources observed during flare stage 2 exhibit distinct emission behaviors and can be divided into two categories. In the two strong (compact) ribbon sources (R2 and R3), WL and mid-IR emissions are closely associated with the HXR and high-frequency microwave radiations, despite a short delay from WL peaks to mid-IR peaks. In contrast, the weak (diffuse) ribbon source and the UN source show brightening in UV, EUV, and mid-IR wavelengths, but exhibit a notable dip in WL emission during the same interval. This result aligns with early findings for flare H and TiO WL radiations (V. Yurchyshyn et al. 2017), mid-IR and HMI/I_c WL emission may not originate in the same chromospheric volume. D.-C. Song et al. (2025) reported 35 s delay from the time derivative of 1–8 Å emission to WL emission near 3600 Å continuum in an X2.8 flare, while we did not find an obvious delay from STIX/HXR to HMI/I_c emission in our event.

The HMI/I_c intensity oscillations in this event were reported by D. Li et al. (2024). Flare peak 2 coincided with an oscillatory minimum, while magnetic reconnection was localized to the compact ribbons (R2 and R3). Nonthermal electrons in these regions produced HXR bursts and HMI/I_c brightening. The diffuse sources (R1 and UN), lying outside the primary reconnection topology, adhered to the background oscillatory pattern and presented dips in WL LCs. The mid-IR emission remained synchronized with UV/EUV. This implies that mid-IR emission does not directly require strong nonthermal electron beams. Instead, it forms at a higher atmospheric layer and can get excited more easily than the HMI/I_c emission. These results advance our understanding of multiwavelength flare diagnostics, particularly the role of mid-IR as a tracer of upper chromospheric energy deposition.

In a previous investigation of an X1.0-class flare (SOL2022-10-02T20:25) accompanied by exceptionally dynamic WL ribbons (X. Yang et al. 2025), the nonthermal electron power reached 8.8×10^{27} erg s^{-1} during the flare peak, as derived from a thick-target bremsstrahlung model incorporating a broken power law with an isothermal component. That X1.0 event presented a peak power two magnitudes lower than that observed in this X6.4 event (3.4×10^{30} erg s^{-1}). The total areas of the HMI/I_c WL kernels were measured as 1.42×10^{17} and 1.29×10^{17} cm^2 for the X1.0 and X6.4 flares, respectively. Thus, the energy flux densities of electrons above 60 keV for the X1.0 and X6.4 flares were 3.10×10^{10} and 1.44×10^{10} erg cm^{-2} s^{-1}, respectively.

Despite our X6.4 flare exhibiting a higher nonthermal electron flux density above 20 keV, the energy flux densities at energies above 60 keV remained at a similar level between the two flares. The comparable high-energy electron flux densities align with similar maximum intensity enhancements (10% of quiet-Sun levels) observed in HMI/I_c. This result is consistent with previous findings that energetic electrons (>50 keV) are more closely associated with WL emission (M. Kuhar et al. 2016; V. Yurchyshyn et al. 2017).

Spectral analysis reveals significantly steeper power-law indices ( ) for the X6.4 flare (= 8.79) compared to the X1.0 event (= 4.30), indicating a higher proportion of high-energy particles in the latter. A flatter energy spectrum in the X1.0 event improves the likelihood of particle penetration into deeper atmospheric layers, with some fraction potentially reaching the temperature minimum region or photosphere (A. J. Monson et al. 2021).

This study presented complex emission sources embedded in complex magnetic configurations. Examining the LCs by integrating the entire multisource flare area risks overlooking key physical information occurring within flare substructures. We resolved the fine-scale evolution of mid-IR flare ribbon R2. It exhibited an apparent speed reaching 76 km s^{-1} in the plane of the sky. Notably, this ribbon evolved within a unipolar magnetic field region, extending along weak-field channels inside the sunspot umbra and penumbra. A plausible explanation for the flare ribbon (R2) extending along weak-field channels could involve the magnetic mirror effect or the magnetic pressure. The magnetic mirror may reflect all flare electrons in the strong-field area and have leakage in the weak-field area. High-resolution HXR imaging is required to better understand this phenomenon. The 30 s delay observed between the HMI/I_c emission and the subsequent 8.2 μm emission was an approximation based on LCs in Figure 3(a3). Accurate measurement would be difficult because the cadence of HMI/I_c is 45 s. The delay between HMI/I_c LC and 10 μm mid-IR LC (by integrating the emission across the whole AR) was not observed in the SOL2017-09-06T12:00 X9.3 flare (C. G. Giménez de Castro et al. 2018).

The observational evidence strongly favors the chromospheric origin of the unidentified mid-IR source. The NLFFF extrapolated magnetic field line configurations (Figure 5, panels (a1) and (a2)) and the potential HXR and microwave source distribution (Figure 5(c1)) describe the footpoint scenario for UN. Numerical calculations from this and prior studies (M. Penn et al. 2016; P. J. A. Simões et al. 2017) indicate that ordinary hydrogen free–free radiation is very unlikely to provide sufficient opacity for mid-IR coronal emission. An exceptionally high electron density ($>10^{12.5}$ cm^{-3}) or an alternative mechanism other than a thermal process may be required to produce the observed mid-IR emission at the flare looptop. As high electron density ($\sim10^{13}$ cm^{-3}) in solar flares was reported before (K. J. H. Phillips et al. 1996; V. Polito et al. 2016), the possibility of the looptop scenario of the UN cannot be entirely ruled out under rare but possibly high electron density situations.

Although, the average apparent speed of the UN exceeded 130 km s^{-1}, which was faster than the typical observed ribbon separation motion in a standard dual-ribbon flare. However, such velocities have been observed as slipping motions in fan-spine ribbon flares (S. Yang et al. 2020) or circular ribbon flares (Y. Shen et al. 2019; Q. Zhang 2024). Notably, the speed of the UN source is also typical for coronal rain (e.g., D. McKenzie 2000). Since the apparent UN motions match those typical of coronal rain, this leads to speculation that higher Z recombination continua might contribute substantial mid-IR opacity in such a source.

Recent studies have reported WL emissions in flare hot loops, both in off-limb observations (J. Zhao et al. 2021; D. Fremstad et al. 2023) and in 1D hydrodynamic loop simulations (K. E. Yang et al. 2023). Although mid-IR flare loops have not yet been directly observed, future limb flare observations will be crucial to confirm the presence of looptop mid-IR emissions.

Acknowledgments

The authors appreciate Dr. Muriel Stiefel from ETH Zurich for processing the SolO/STIX HXR data. This study benefited from scientific discussions with Dr. Bin Chen and Dr. Yan Xu from New Jersey Institute of Technology (NJIT). The quantitative analysis for mid-IR emission benefited from support by Dr. Guigue Giménez de Castro at Universidade Presbiteriana Mackenzie. The authors appreciate the use of data from the Goode Solar Telescope (GST) of the Big Bear Solar Observatory (BBSO). The operation of BBSO is supported by the US NSF AGS-2309939 grant and NJIT. GST operation is partly supported by the Korea Astronomy and Space Science Institute and the Seoul National University. The Expanded Owens Valley Solar Array (EOVSA) was designed and built and is now operated by NJIT as a community facility. EOVSA operations are supported by NSF grant AGS-2130832 to NJIT. V.Y. and W.C. are supported by NSF grants AGS-2401229, 2309939 and 2408174, AST-2108235, and NASA grant 80NSSC24K1914. J.Q. is supported by NSF grants AST-2407849 and AGS-2401228. P.J.A.S. acknowledges support from CNPq 305808/2022-2, MackPesquisa 231017, and FAPESP 2022/15700-7 grants. S.M.P. acknowledges financial support from CAPES PROSUC. L.F. acknowledges the support of grants ST/T000422/1 and ST/X000990/1 made by the UK Research and Innovation's Science and Technology Facilities Council. H.H. is grateful for the hospitality at the University of Glasgow.

Facilities: GST (MIRI), EOVSA, SDO (AIA and HMI), SolO (STIX).

Author Contributions

X.Y. calibrated, reduced, and analyzed all data. W.C. led the campaign to obtain observational data. M.W. reduced HXR and microwave data and inverted the energy flux of flare nonthermal electrons. W.H. made the NLFFF extrapolation. D. J., M.J., and A.L. commissioned the mid-IR instrument and instructed the observation. J.Q., V.Y., H.H., and D.J. provided scientific consultation. All authors participated in the discussion.

X.Y., W.C., and M.W. were responsible for writing and submitting the manuscript. All authors edited the manuscript.

ORCID iDs

Xu Yang https://orcid.org/0000-0002-3238-0779
Wenda Cao https://orcid.org/0000-0003-2427-6047
Meiqi Wang https://orcid.org/0000-0002-2633-3562
Jiong Qiu https://orcid.org/0000-0002-2797-744X
Wen He https://orcid.org/0000-0001-8749-1022
Solomon M. Perriyil https://orcid.org/0009-0002-6257-3034
Vasyl Yurchyshyn https://orcid.org/0000-0001-9982-2175
Lyndsay Fletcher https://orcid.org/0000-0001-9315-7899
Paulo J. A. Simões https://orcid.org/0000-0002-4819-1884
Xingyao Chen https://orcid.org/0000-0002-1810-6706
Hugh Hudson https://orcid.org/0000-0001-5685-1283

References

Atwood, W. B., Abdo, A. A., Ackermann, M., et al. 2009, ApJ, 697, 1071
Bobra, M. G., Sun, X., Hoeksema, J. T., et al. 2014, SoPh, 289, 3549
Brown, J. C. 1971, SoPh, 18, 489
Bundas, J., Patnaude, K., Dennis, R., et al. 2006, Proc. SPIE, 6206, 62060G
Carlsson, M., & Stein, R. F. 1992, ApJ, 397, L59
Fletcher, L., Dennis, B. R., Hudson, H. S., et al. 2011, SSRv, 159, 19
Fremstad, D., Guevara Gómez, J. C., Hudson, H., & Martínez Oliveros, J. C. 2023, A&A, 672, A32
Gary, D. E., Chen, B., Dennis, B. R., et al. 2018, ApJ, 863, 83
Giménez de Castro, C. G., Raulin, J., Valle Silva, J. F., et al. 2018, SpWea, 16, 1261
Goode, P. R., & Cao, W. 2012, Proc. SPIE, 8444, 844403
He, W., Hu, Q., Jiang, C., Qiu, J., & Prasad, A. 2022, ApJ, 934, 103
Heinzel, P., Kleint, L., Kašparová, J., & Krucker, S. 2017, ApJ, 847, 48
Holman, G. D., Aschwanden, M. J., Aurass, H., et al. 2011, SSRv, 159, 107
Jejcic, S., Kleint, L., & Heinzel, P. 2018, ApJ, 867, 134
Jiang, C., & Feng, X. 2013, ApJ, 769, 144
Jiang, C., Feng, X., Fan, Y., & Xiang, C. 2011, ApJ, 727, 101
Kaufmann, P., White, S. M., Freeland, S. L., et al. 2013, ApJ, 768, 134
Kleint, L., Heinzel, P., Judge, P., & Krucker, S. 2016, ApJ, 816, 88
Krucker, S., Hurford, G. J., Grimm, O., et al. 2020, A&A, 642, A15
Kudaka, A. S., Cassiano, M. M., Marcon, R., et al. 2015, SoPh, 290, 2373
Kuhar, M., Krucker, S., Oliveros, J. C. M., et al. 2016, ApJ, 816, 6
Lemen, J. R., Title, A. M., Akin, D. J., et al. 2011, SoPh, 275, 17
Li, D., Wang, J., & Huang, Y. 2024, ApJL, 972, L2
López, F. M., Giménez de Castro, C. G., Mandrini, C. H., et al. 2022, A&A, 657, A51
Massa, P., Schwartz, R., Tolbert, A. K., et al. 2020, ApJ, 894, 46
McKenzie, D. 2000, SoPh, 195, 381
McMullin, J. P., Waters, B., Schiebel, D., Young, W., & Golap, K. 2007, in ASP Conf. Ser. 376, Astronomical Data Analysis Software and Systems XVI, ed. R. A. Shaw, F. Hill, & D. J. Bell (San Francisco, CA: ASP), 127
Miteva, R., Kaufmann, P., Cabezas, D. P., et al. 2016, A&A, 586, A91

Monson, A. J., Mathioudakis, M., Reid, A., Milligan, R., & Kuridze, D. 2021, ApJ, 915, 16
Neidig, D. 1989, SoPh, 121
Ohki, K., & Hudson, H. S. 1975, SoPh, 43, 405
Penn, M., Krucker, S., Hudson, H., et al. 2016, ApJL, 819, L30
Phillips, K. J. H., Bhatia, A. K., Mason, H. E., & Zarro, D. M. 1996, ApJ, 466, 549
Polito, V., Del Zanna, G., Dudík, J., et al. 2016, A&A, 594, A64
Roy, S., Tripathi, D., Padinhatteeri, S., et al. 2025, ApJL, 981, L19
Scherrer, P. H., Schou, J., Bush, R. I., et al. 2011, SoPh, 275, 207
Schou, J., Scherrer, P. H., Bush, R. I., et al. 2011, SoPh, 275, 229
Schwartz, R., Csillaghy, A., Tolbert, A., et al. 2002, SoPh, 210, 165
Shen, Y., Qu, Z., Zhou, C., et al. 2019, ApJL, 885, L11
Silva, A. V. R., Wang, H., & Gary, D. E. 2000, ApJ, 545, 1116
Simões, P. J. A., Fletcher, L., Hudson, H. S., et al. 2024, MNRAS, 532, 705
Simões, P. J. A., Kerr, G. S., Fletcher, L., et al. 2017, A&A, 605, A125
Song, D.-C., Dominique, M., Zimovets, I., et al. 2025, ApJL, 983, L41
Trottet, G., Raulin, J.-P., Mackinnon, A., et al. 2015, SoPh, 290, 2809
Wiegelmann, T., Inhester, B., & Sakurai, T. 2006, SoPh, 233, 215
Xu, Y., Cao, W., Liu, C., et al. 2004, ApJ, 607, L131
Yang, K. E., Sun, X., Kerr, G. S., & Hudson, H. S. 2023, ApJ, 959, 54
Yang, S., Zhang, Q., Xu, Z., et al. 2020, ApJ, 898, 101
Yang, X., Cao, W., & Yurchyshyn, V. 2022, ApJS, 262, 55
Yang, X., Wang, M., Cao, A., et al. 2025, ApJL, 979, L43
Yurchyshyn, V., Kumar, P., Abramenko, V., et al. 2017, ApJ, 838, 32
Zhang, Q. 2024, RvMPP, 8, 7
Zhao, J., Liu, W., & Vial, J.-C. 2021, ApJL, 921, L26